JACS
JOURNAL OF THE AMERICAN CHEMICAL SOCIETY

Communication

pubs.acs.org/JACS

Perovskite Solar Cells with Near 100% Internal Quantum Efficiency Based on Large Single Crystalline Grains and Vertical Bulk Heterojunctions

Bin Yang,[†] Ondrej Dyck,[‡] Jonathan Poplawsky,[†] Jong Keum,[†] Alexander Puretzky,[†] Sanjib Das,[§] Ilia Ivanov,[†] Christopher Rouleau,[†] Gerd Duscher,[‡] David Geohegan,[†] and Kai Xiao*[,†]

[†]Center for Nanophase Materials Sciences, Oak Ridge National Laboratory, Oak Ridge, Tennessee 37831, United States
[‡]Department of Materials Science and Engineering, University of Tennessee, Knoxville, Tennessee 37996, United States
[§]Department of Electrical Engineering and Computer Science, University of Tennessee, Knoxville, Tennessee 37996, United States

Supporting Information

ABSTRACT: Imperfections in organometal halide perovskite films such as grain boundaries (GBs), defects, and traps detrimentally cause significant nonradiative recombination energy loss and decreased power conversion efficiency (PCE) in solar cells. Here, a simple layer-by-layer fabrication process based on air exposure followed by thermal annealing is reported to grow perovskite films with large, single-crystal grains and vertically oriented GBs. The hole-transport medium Spiro-OMeTAD is then infiltrated into the GBs to form vertically aligned bulk heterojunctions. Due to the space-charge regions in the vicinity of GBs, the nonradiative recombination in GBs is significantly suppressed. The GBs become active carrier collection channels. Thus, the internal quantum efficiencies of the devices approach 100% in the visible spectrum range. The optimized cells yield an average PCE of 16.3 ± 0.9%, comparable to the best solution-processed perovskite devices, establishing them as important alternatives to growing ideal single crystal thin films in the pursuit toward theoretical maximum PCE with industrially realistic processing techniques.

Organometal halide perovskites exhibit great promise for low-cost and high-efficiency thin film solar cells due to the relative ease through solution casting to achieve high degrees of crystallinity,[1] excellent carrier transport properties,[2] tunable optical band gaps,[3] and strong light absorption.[4] The methylammonium lead trihalide perovskites, such as $CH_3NH_3PbI_3$ and $CH_3NH_3PbBr_3$, were initially applied to develop sensitized liquid junction photovoltaic devices.[5] The demonstration of the robust solid state perovskite cells with power conversion efficiency (PCE) exceeding 9% and long-term stability[6] stimulated significant research interests in these high-performance hybrid perovskites, leading to a high certified PCE of ~20% in about three years.[1,4a,7] Recent works propose that the primary energy loss in hybrid perovskite solar cells is caused by the nonradiative recombination of carriers due to trap states at grain boundaries (GBs) and surfaces as well as point defects, such as interstitial defects or vacancies, in the perovskite crystal lattice.[2,8] Therefore, overcoming nonradiative recombination in perovskite thin film devices has concentrated on obtaining large crystallites within films, with low densities of GBs and intragranular defects,[8a,c,9] as well as on passivating the GB defect states.[8b] Ideally, growth of single crystal perovskite films would completely remove the above-mentioned imperfections to suppress energetic disorder and nonradiative recombination losses, to enable organometal halide perovskite photovoltaics with PCE approaching the Shockley−Queisser maxima of ~30%.[10] Very recently, millimeter-scale methylammonium lead trihalide perovskite single crystals have been developed using a solution method.[2,11] However, direct growth of single crystal perovskite thin films on titanium dioxide (TiO_2) coated substrates is very challenging. Additionally, the conventional solution-based single-step processing is very difficult to achieve perfect single crystal perovskite thin films due to the fast chemical reaction between lead iodide (PbI_2) and methylammonium iodide (CH_3NH_3I) precursors that produces a large quantity of stable $CH_3NH_3PbI_3$ seed clusters.[4a] These seed clusters tend to nucleate multiple grains during the crystallization process.

In this work, we grew perovskite thin films with large single crystalline grains and vertically oriented grain boundaries through a simple solution-based layer-by-layer spin-coating method followed by air exposure and thermal annealing treatments. The GBs were shown to be infiltrated with p-type doped 2,2′,7,7′-tetrakis[*N*,*N*-di(*p*-methoxyphenylamine)]-9,9-spirobifluorene (Spiro-OMeTAD) to form a new type of vertical bulk heterojunction (BHJ) structure within the perovskite films as demonstrated by electron energy loss spectroscopy (EELS) study and electron beam induced current (EBIC) mapping. These measurements also showed that the BHJs at GBs can significantly reduce nonradiative recombination losses as well as enhance carrier collection in the devices. This approach leads to high performance devices with near 100% internal quantum efficiencies (IQEs) in the visible light range and high average PCE of 16.3 ± 0.9%.

We applied a sequential spin-coating method to fabricate the PbI_2/CH_3NH_3I bilayer films in a N_2-filled glovebox. The as-casted bilayer films were initially exposed in ambient air (humidity of ~30%) during the chemical formation of the

Received: April 2, 2015
Published: July 9, 2015

DOI: 10.1021/jacs.5b03144
J. Am. Chem. Soc. 2015, 137, 9210−9213

perovskite layers. X-ray diffraction (XRD) was employed to examine the chemical reaction between the two precursor layers (PbI_2/CH_3NH_3I) during room-temperature air exposure. We found that the spin-coated PbI_2/CH_3NH_3I bilayer film completely converts into a polycrystalline perovskite film after air exposure for 60 min, as shown by the disappearance of the PbI_2 Bragg peaks (blue XRD pattern in Figure 1a) and

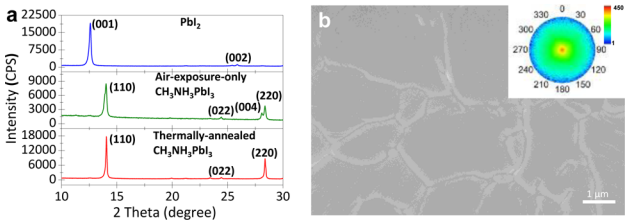

Figure 1. (a) XRD patterns of original PbI_2 film (blue pattern, top), PbI_2/CH_3NH_3I bilayer film air-exposed for 60 min at room temperature (olive pattern, middle), and thermally annealed perovskite film for 2 h at 100 °C (red pattern, bottom). An SEM image shows the surface morphologies of 2 h annealed perovskite film. Inset of (b) shows the corresponding X-ray pole figure for the (110) plane of the $CH_3NH_3PbI_3$ crystal.

appearance of the $CH_3NH_3PbI_3$ Bragg peaks (olive XRD pattern in Figure 1a). It is clear from the data that the chemical reaction of PbI_2/CH_3NH_3I and crystallization of perovskites can occur even without thermal annealing to drive interdiffusion between PbI_2 and CH_3NH_3I, which may be due to formation of a more reactive intermediate phase $CH_3NH_3PbI_3{\cdot}H_2O$ during air exposure at room temperature.[12] A subsequent treatment of 100 °C thermal annealing results in a 2-fold increase in the (110) peak intensity and narrows down the (110) peak width (red XRD pattern in Figure 1a), which indicates significantly enhanced crystallinity in air-exposure-only perovskite films. Scanning electron microscopy (SEM) imaging shows that grains larger than 2 μm in the lateral direction are observed after annealing for 2 h (Figure 1b). The X-ray pole figure measurement was used to probe the global orientation and crystallographic texture of the perovskite crystals, which clearly indicates that the grains in 2 h annealed perovskite films show excellent orientation, as suggested by a maxima orientation of [110] (the inset of Figure 1b). Ambient-air exposure is one significant factor to grow large single crystalline grains, which appear to be larger than the grains in the nonair-exposure perovskite films (Figure S1).

We then applied the large perovskite grain films, as shown in Figure 1b, to make solar cells. The typical device yields a short-circuit current density (J_{SC}) of 21.9 mA/cm^2, an open-circuit voltage (V_{OC}) of 1.041 V, a fill factor (FF) of 73.5%, and a PCE of 16.8% (Figure 2a), when measured by sweeping from forward bias (1.2 V) to reverse bias (−0.2 V). Negligible J−V hysteresis is observed from this device when scanning from forward bias (1.2 V) to reverse bias (−0.2 V) and from reverse bias (−0.2 V) to forward bias (1.2 V), with a 50 ms sweep delay time, as shown in Figure S2. Nevertheless, a hysteresis emerges using a longer sweep delay time, such as 800 ms. This result suggests that the hysteresis is dependent on the sweep delay time (or scan rate) in our planar heterojunction configuration devices, which is consistent with that reported by Snaith et al.,[13] but opposite to the variation trend observed in mesoporous TiO_2 configuration devices reported by Seok et al.[4b] and Dualeh et al.,[14] where the hysteresis was found to be reduced as

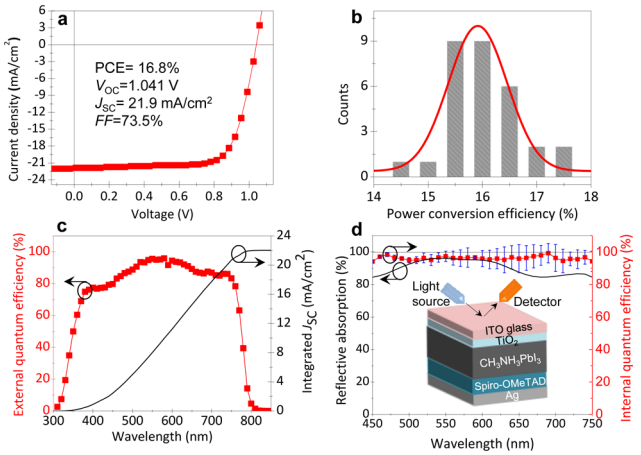

Figure 2. (a) J−V curve of a device under illumination of 100 mW/cm^2. (b) A Gaussian distribution of the ∼30 device efficiencies. (c) External quantum efficiency (EQE) and integrated short circuit current density (J_{SC}) versus wavelength. (d) Reflective absorption and internal quantum efficiency (IQE) versus wavelength. Inset illustration shows the reflective absorption measurement setup.

the scan rate decreased. The origin of the sweep-rate dependent J−V hysteresis in our devices may be attributed to two major theories: (1) trap states within or close to the surface of the perovskites, which induce the trapping/detrapping process of charge carriers,[8b,13] and (2) ion migration in perovskite films under applied electric fields, such as Pb^{2+}, I^-.[15] A Gaussian distribution of device efficiencies based on ∼30 devices is shown in Figure 2b, with a mean PCE of 16.3 ± 0.9%. We also measured external quantum efficiencies (EQEs) of these devices. A typical EQE curve was shown in Figure 2c. The EQE spectrum integration over the AM 1.5 G solar spectrum (100 mW/cm^2) yields a J_{SC} of ∼22 mA/cm^2 (Figure 2c), which is consistent with the J_{SC} obtained from the J−V sweep. To further examine the IQE, the absorption spectrum was measured in reflectance, mimicking the light absorption process in real devices, as depicted in the inset of Figure 2d. It is remarkable that the IQE, calculated by dividing the EQE by the reflective absorption, approaches 100% from 450 to 750 nm (Figure 2d).

IQEs near 100% evidence remarkable carrier generation and collection efficiencies in our devices. In order to reveal the origin of the exceptional cell performance, we first investigated the vertical microstructure of the perovskite film in the devices. Transmission electron microscopy (TEM) was applied to image the cross-sectional morphology of the entire device with architecture ($ITO/TiO_2/CH_3NH_3PbI_3/Spiro\text{-}OMeTAD/Ag$). Large oriented-crystalline grains and vertically aligned GBs were clearly identified (Figure 3a). Similar crystallographic orientations along the direction parallel to the substrate were observed, as shown by two typical selected area electron diffraction (SAED) patterns acquired in two separate grains (patterns 1 and 3); Pattern 2 is a superposition of patterns 1 and 3 as the SAED was taken across the GB (Figure 3a). The lateral size of typical single crystal domains exceeds our aperture size of 325 nm, which makes electrons easily illuminating single crystal regions. To investigate the vertical single crystal grain size, a smaller SAED aperture with a 180 nm diameter was inserted and used to acquire a series of very similar SAED patterns (patterns 4, 5, and 6) perpendicular to the film substrate through the entire ∼450-nm-thick perovskite

DOI: 10.1021/jacs.5b03144
J. Am. Chem. Soc. 2015, 137, 9210−9213

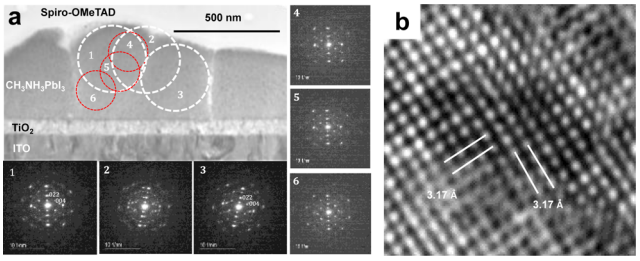

Figure 3. (a) Cross-sectional bright field TEM images show vertical phase morphologies of a device. The inset SAED patterns demonstrate large single crystal grains in perovskite thin film; Patterns 1–3 (white dotted circles) and patterns 4–6 (red dotted circles) were taken along the parallel and perpendicular direction to the ITO substrate, respectively. (b) An atomic resolution TEM shows a lattice spacing of 3.17 Å.

layer. The results suggest that a single crystal domain crosses the entire film in the perpendicular direction. An atomic resolution TEM image (Figure 3b) shows clear lattice fringes indicating the formation of a crystalline structure with a lattice spacing of 3.17 Å, which could be indexed as (220) of the tetragonal $CH_3NH_3PbI_3$ phase.[16] High resolution TEM/SAED studies clearly show a high degree of crystallinity and a low density of GBs in our perovskite films, which could be one reason for excellent carrier generation and collection efficiencies.

EBIC measurements were further applied to reveal local electrical properties in single crystal grains as well as vertical GBs within the active layer. In EBIC, highly energetic electrons are used to generate several electron–hole pairs in targeted areas of a semiconductor, which are separated due to internal electric fields and collected at electrodes. By scanning the electron beam, EBIC measurements reveal several important electrical characteristics, such as the presence of internal electric fields, the location of p–n junctions at the mesoscopic scale, recombination centers (e.g., grain boundaries), and estimation of minority carrier diffusion lengths.[17] Figure 4a shows a cross-sectional SEM image and corresponding EBIC image of a device. The line profiles of the cross-sectional SEM image and EBIC image are presented in Figure 4b. It is clear from these data that electrical current is generated throughout the entire perovskite active layer, which is indicative of p-i-n structure.[18] Moreover, the EBIC signal in the GB region is stronger compared to the grain regions (Figure 4a). A line profile of EBIC current across a typical GB between two $CH_3NH_3PbI_3$ grains shows that an about 70% higher EBIC current was measured in the vicinity of the GB with respect to the surrounding grains (Figure 4c), which implies that the GBs are active channels for carrier separation and collection rather than strong recombination regions.

In order to understand the underlying causes of superior carrier collections in GBs, we need to unveil the presence of materials in the GBs. Thus, we examined the GBs between these vertically aligned single-crystalline grains with Z-contrast scanning transmission electron microscopy (Z-STEM) and EELS mapping. Figure 4d shows the cross-sectional morphology of two $CH_3NH_3PbI_3$ grains and a vertical GB. Since iodine is only present in $CH_3NH_3PbI_3$, CH_3NH_3I, and PbI_2, and both carbon and nitrogen are rich in organic material Spiro-OMeTAD, we thereby acquired EELS mapping images of iodine (Figure 4e), carbon (Figure 4f), and nitrogen (Figure 4g) atomic areal densities. A magnified GB from a similar sample and corresponding EELS map images are also shown in Figure S3. The evidence of poor iodine and rich carbon and rich nitrogen in GBs compared to the surrounding grains indicates that the Spiro-OMeTAD is most likely infiltrated in the boundaries. Moreover, the infiltration of Spiro-OMeTAD in GBs would form BHJs between perovskite grains and GBs within the active layer. The enhancement in carrier collection could be ascribed to BHJs between perovskite grains and p-type doped Spiro-OMeTAD filled GBs. The space charge regions

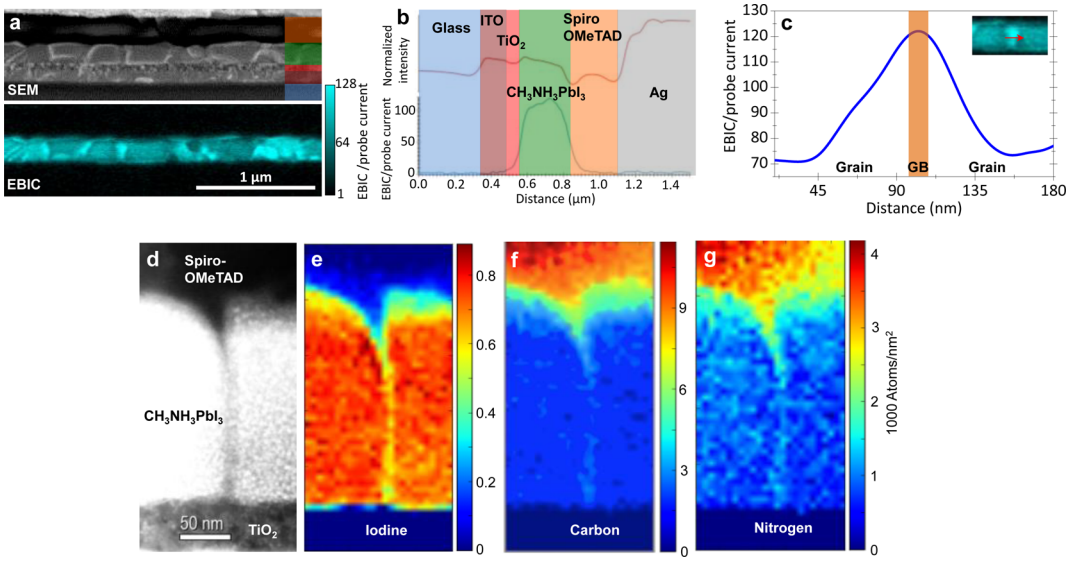

Figure 4. (a) Cross-sectional SEM image (up) and corresponding EBIC image (down) of a device. (b) The corresponding line profiles of the cross-sectional SEM image (up, red curve) and EBIC image (down, green curve) at the indicated regions as shown in the inset. (c) Line profile of EBIC current across the GBs between two $CH_3NH_3PbI_3$ grains, which was taken in the location as shown in the inset image. A Z-contrast dark-field STEM image (d) and corresponding EELS maps (e–g) demonstrate a GB infiltrated with Spiro-OMeTAD between two $CH_3NH_3PbI_3$ grains. The atomic areal density elemental maps (e, iodine; f, carbon; and g, nitrogen) show significant rich content of both carbon and nitrogen and poor iodine in GBs.

DOI: 10.1021/jacs.5b03144
J. Am. Chem. Soc. 2015, 137, 9210–9213

between the $CH_3NH_3PbI_3$ grains separate photogenerated electron–hole pairs and suppress the carrier recombination loss.[17] The Spiro-OMeTAD filled GB is a good pathway to allow the holes to travel with less resistance to the device back contact. Therefore, the remarkable near 100% IQE of our devices is most likely due to the combination effect of large single crystal grains and vertical BHJs. Moreover, the suppressed J–V hysteresis in our devices may result from (1) reduction of trap density due to growth of large single-crystalline grains[13] and (2) passivation of trap states of the perovskites by infiltration of Spiro-OMeTAD into GBs.[8b] We note that the GBs are only partially infiltrated with Spiro-OMeTAD. It is thus expected that, with increasing the infiltration of Spiro-OMeTAD into GBs, the J–V hysteresis could be further reduced and the V_{OC} would be further enhanced to exceed 1.1 V in $CH_3NH_3PbI_3$ perovskites based solar cells.

In summary, we have obtained a high PCE of 16.3 ± 0.9% based on perovskite thin films containing large single-crystal grains and vertical GBs. We have demonstrated the hole transport medium Spiro-OMeTAD is infiltrated into the GBs to form vertical BHJs within a perovskite layer to suppress the recombination loss and enhance carrier collection in the vicinity of GBs, leading to IQEs approaching 100%. Our approach presents a facile and important alternative pathway to achieve the theoretical maximum PCE in hybrid perovskite solar cells.

■ ASSOCIATED CONTENT

Supporting Information

Details of materials preparation, device fabrication, XRD, TEM, EELS, and EBIC characterizations; SEM images of $CH_3NH_3PbI_3$ film with and without air exposure; Hysteresis of J–V curves; high magnification STEM image and EELS maps in vicinity of a GB. The Supporting Information is available free of charge on the ACS Publications website at DOI: 10.1021/jacs.5b03144.

■ AUTHOR INFORMATION

Corresponding Author

*E-mail: xiaok@ornl.gov.

Notes

The authors declare no competing financial interest.

■ ACKNOWLEDGMENTS

This research was conducted at the Center for Nanophase Materials Sciences (CNMS), which is a DOE Office of Science User Facility.

■ REFERENCES

(1) Liu, M.; Johnston, M. B.; Snaith, H. J. *Nature* **2013**, *501*, 395–398.
(2) Dong, Q.; Fang, Y.; Shao, Y.; Mulligan, P.; Qiu, J.; Cao, L.; Huang, J. *Science* **2015**, *347*, 967–970.
(3) Hao, F.; Stoumpos, C. C.; Cao, D. H.; Chang, R. P. H.; Kanatzidis, M. G. *Nat. Photonics* **2014**, *8*, 489–494.
(4) (a) Burschka, J.; Pellet, N.; Moon, S.-J.; Humphry-Baker, R.; Gao, P.; Nazeeruddin, M. K.; Grätzel, M. *Nature* **2013**, *499*, 316–319. (b) Jeon, N. J.; Noh, J. H.; Kim, Y. C.; Yang, W. S.; Ryu, S.; Seok, S. I. *Nat. Mater.* **2014**, *13*, 897–903.
(5) (a) Kojima, A.; Teshima, K.; Shirai, Y.; Miyasaka, T. *J. Am. Chem. Soc.* **2009**, *131*, 6050–6051. (b) Im, J.-H.; Lee, C.-R.; Lee, J.-W.; Park, S.-W.; Park, N.-G. *Nanoscale* **2011**, *3*, 4088–4093.
(6) Kim, H.-S.; Lee, C.-R.; Im, J.-H.; Lee, K.-B.; Moehl, T.; Marchioro, A.; Moon, S.-J.; Humphry-Baker, R.; Yum, J.-H.; Moser, J. E.; Grätzel, M.; Park, N.-G. *Sci. Rep.* **2012**, *2*, 591.
(7) Yang, W. S.; Noh, J. H.; Jeon, N. J.; Kim, Y. C.; Ryu, S.; Seo, J.; Seok, S. I. *Science* **2015**, *348*, 1234–1237.
(8) (a) Nie, W.; Tsai, H.; Asadpour, R.; Blancon, J.-C.; Neukirch, A. J.; Gupta, G.; Crochet, J. J.; Chhowalla, M.; Tretiak, S.; Alam, M. A.; Wang, H.-L.; Mohite, A. D. *Science* **2015**, *347*, 522–525. (b) Shao, Y.; Xiao, Z.; Bi, C.; Yuan, Y.; Huang, J. *Nat. Commun.* **2014**, *5*, 5784. (c) Zhao, D.; Sexton, M.; Park, H. Y.; Baure, G.; Nino, J. C.; So, F. *Adv. Energy Mater.* **2015**, *5*, 1401855.
(9) Im, J.-H.; Jang, I.-H.; Pellet, N.; Grätzel, M.; Park, N.-G. *Nat. Nanotechnol.* **2014**, *9*, 927–932.
(10) Shockley, W.; Queisser, H. J. *J. Appl. Phys.* **1961**, *32*, 510–519.
(11) Shi, D.; Adinolfi, V.; Comin, R.; Yuan, M.; Alarousu, E.; Buin, A.; Chen, Y.; Hoogland, S.; Rothenberger, A.; Katsiev, K.; Losovyj, Y.; Zhang, X.; Dowben, P. A.; Mohammed, O. F.; Sargent, E. H.; Bakr, O. M. *Science* **2015**, *347*, 519–522.
(12) (a) Hao, F.; Stoumpos, C. C.; Liu, Z.; Chang, R. P.; Kanatzidis, M. G. *J. Am. Chem. Soc.* **2014**, *136*, 16411–16419. (b) Zhou, H.; Chen, Q.; Li, G.; Luo, S.; Song, T.-b.; Duan, H.-S.; Hong, Z.; You, J.; Liu, Y.; Yang, Y. *Science* **2014**, *345*, 542–546.
(13) Snaith, H. J.; Abate, A.; Ball, J. M.; Eperon, G. E.; Leijtens, T.; Noel, N. K.; Stranks, S. D.; Wang, J. T.-W.; Wojciechowski, K.; Zhang, W. *J. Phys. Chem. Lett.* **2014**, *5*, 1511–1515.
(14) Dualeh, A.; Moehl, T.; Tétreault, N.; Teuscher, J.; Gao, P.; Nazeeruddin, M. K.; Grätzel, M. *ACS Nano* **2014**, *8*, 362–373.
(15) Xiao, Z.; Yuan, Y.; Shao, Y.; Wang, Q.; Dong, Q.; Bi, C.; Sharma, P.; Gruverman, A.; Huang, J. *Nat. Mater.* **2015**, *14*, 193–198.
(16) Baikie, T.; Fang, Y.; Kadro, J. M.; Schreyer, M.; Wei, F.; Mhaisalkar, S. G.; Graetzel, M.; White, T. J.; Pennycook, S. J.; Yan, Y. *J. Mater. Chem. A* **2013**, *1*, 5628–5641.
(17) Li, C.; Wu, Y.; Poplawsky, J.; Pennycook, T. J.; Paudel, N.; Yin, W.; Haigh, S. J.; Oxley, M. P.; Lupini, A. R.; Al-Jassim, M. *Phys. Rev. Lett.* **2014**, *112*, 156103.
(18) Edri, E.; Kirmayer, S.; Mukhopadhyay, S.; Gartsman, K.; Hodes, G.; Cahen, D. *Nat. Commun.* **2014**, *5*, 3461.

DOI: 10.1021/jacs.5b03144
J. Am. Chem. Soc. 2015, 137, 9210–9213